J. Fluid Mech. (2008), *vol.* 615, *pp.* 27–51. © 2008 Cambridge University Press
doi:10.1017/S0022112008003480 Printed in the United Kingdom

The lift force on a bubble in a sheared suspension in a slightly inclined channel

XIAOLONG YIN AND DONALD L. KOCH

School of Chemical and Biomolecular Engineering, Cornell University, 120 Olin Hall, Ithaca, NY 14853, USA

(Received 13 January 2007 and in revised form 14 July 2008)

The lattice Boltzmann method was applied to simulate the free rise of monodisperse non-coalescing spherical bubbles in slightly inclined channels bound by solid walls. The Reynolds number based on the relative velocity between the bubbles and the fluid ranged from 4 to 16, the volume fraction from 5 % to 10 % and the inclination angle from 2° to 6°. The simulations revealed that the weak buoyancy component normal to the walls led to a layer of bubbles near the upper wall and a depleted layer near the bottom wall. These thin layers drove a nearly viscometric shear flow within the bulk of the channel that allowed an unambiguous determination of the lift force in a sheared homogeneous and freely evolving bubble suspension. The lift force coefficients calculated from our simulations were always higher than those for isolated spherical bubbles, suggesting that the lift force is enhanced by hydrodynamic interactions among the bubbles. Experimental measurements of the velocity gradient in 10 % volume fraction bubble suspensions in glycerine–water–electrolyte mixtures in slightly inclined channels yielded lift coefficients in excess of those predicted for isolated bubbles and confirmed the qualitative predictions of the simulations.

1. Introduction

It is well known that a bubble moving in a shear flow will experience a transverse force known as the lift force. The lift force on a bubble can be attributed to the inertia of the fluid, the deformation of the bubble or an uneven distribution of surface tension. In this study, we restricted ourselves to spherical bubbles with clean surfaces, i.e. surfaces with zero-shear-stress boundary condition. For such bubbles, the lift force is strictly an inertial effect, because the reversibility of Stokes flows does not allow a force to occur in the transverse direction. The lift force acting on an isolated spherical bubble with a clean surface as a function of Reynolds number and local shear rate has been well characterized in a series of theoretical and numerical studies (Lighthill 1956; Auton 1987; Legendre & Magnaudet 1997, 1998). These theories can be applied to the motion of bubbles in flows with strong velocity gradients, e.g. in pipes, near walls, and in turbulent vortices. However, equations of motion using lift coefficients for isolated bubbles (e.g. Magnaudet & Eames 2000) are only accurate when the suspension of interest is dilute. In non-dilute bubble suspensions, the lift force will have a dependence on the bubble volume fraction ϕ due to bubble–bubble hydrodynamic interaction. This volume-fraction dependence of the lift force, though practically important, has not been explored in detail in the past due to the difficulties in isolating the lift force from all the other factors affecting bubble motions in experiments and simulations. In this study, we used a slightly inclined

channel to generate a nearly viscometric shear flow in a homogeneous monodisperse bubble suspension, where the lift force was balanced by the buoyancy force normal to the walls and all other terms in the transverse dispersed phase momentum equation were zero. Using this setup, we conducted numerical simulations and experiments and characterized the dependence of the lift force on bubble concentration in a disordered system of freely suspended bubbles.

A spherical bubble embedded in a simple shear flow with a fluid velocity $\boldsymbol{u} = \boldsymbol{e}_x \alpha y$ experiences a lift force $\boldsymbol{e}_y F_L$, where

$$F_L = -\frac{\rho \pi d^3}{6} C_L U_r \alpha, \tag{1.1}$$

in which U_r (> 0) is the velocity of the bubble relative to the fluid and is in the direction of $\boldsymbol{e}_x$; ρ is the fluid density; d is the bubble diameter; and C_L is the lift force coefficient. In the subsequent discussion we will use C_L^* to denote the lift coefficient in a bubble suspension and C_L to denote the lift coefficient of an isolated bubble. The important non-dimensional numbers in our simulations are the Reynolds number, defined as $Re = \rho U_r d/\eta$ with η the viscosity of the fluid, and the ratio of shear to relative velocity $Sr = |\alpha| d/U_r$.

Analytical determination of C_L as a function of Re and Sr, due to the three-dimensional nature of the problem, is not trivial and is limited to flows with either very high Reynolds numbers, where a weak shear is superimposed on a potential flow field (e.g. Lighthill 1956; Auton 1987), or flows with very low but still finite Reynolds numbers, where the effects of inertia and shear can be considered perturbations (e.g. Saffman 1965; McLaughlin 1991; Legendre & Magnaudet 1997). In the intermediate Re regime, C_L was determined numerically by Legendre & Magnaudet (1998) in the range $0.1 < Re < 500$ and $0.02 < Sr < 1$, and the results are summarized into the expression

$$C_L = \left\{ \left[\frac{1.879}{Re\, Sr (1 + 0.2 Re/Sr)^3} \right] + \left[\left(\frac{1}{2} \right) \left(\frac{1 + 16 Re^{-1}}{1 + 29 Re^{-1}} \right) \right]^2 \right\}^{1/2} \tag{1.2}$$

that correctly bridges the low Re limit derived by Legendre & Magnaudet (1997) and the high Re limit, $C_L = 1/2$, derived by Auton (1987).

Compared to numerical simulations, experimental determination of the lift force F_L and the lift force coefficient C_L is much more difficult, because it requires a clever design of the experiments in which the lift force is balanced by other measurable forces as well as a tight control of experimental conditions to ensure the bubbles do not deform or suffer contamination by surfactants. A few experimental attempts have been made to characterize the lift force on an isolated bubble. For example Sridhar & Katz (1995) designed an experiment to track the motions of small bubbles entrained in vortices (0.5–0.8 mm, $20 < Re < 80$) and measured the drag and lift forces on the bubbles. Rensen *et al.* (2001) found that under the action of acoustic forces, a bubble in a shear flow undergoes a spiralling motion, which in principle could be used to determine the lift force. The most recent experimental study by Van Nierop *et al.* (2007) used a solid-body rotation of the liquid to control the motion of a small and essentially spherical bubble ($\sim$1 mm) and calculated the drag and lift forces using a simplified equation of motion proposed by Magnaudet & Eames (2000). The accuracy of these experiments, however, still needs to be improved: the effect of surfactant contamination was not completely ruled out, and determining the drag and lift forces from the trajectory of a bubble using a simplified equation of motion

generated fairly significant experimental errors. Moreover, these techniques cannot be easily adapted to a sheared bubble suspension to measure the average lift force and the associated C_L^*.

In this study, we use a combination of numerical simulations and experiments to characterize the average lift force acting on spherical bubbles in a simple shear flow. Generally speaking, bubbles would remain spherical if the relevant dimensionless numbers – the Eötvös number $Eo = |\boldsymbol{g}|\rho d^2/\sigma$ that compares buoyancy to surface tension, the capillary number $Ca = \eta|\alpha|d/\sigma$ that compares shear to surface tension and the Weber number $We = \rho U_r^2 d/\sigma$ that compares inertia to surface tension – are sufficiently small. Here $\boldsymbol{g}$ is the gravitational acceleration, and σ is the surface tension. Another parameter that characterizes the properties of the fluid is the Morton number $Mo = |\boldsymbol{g}|\eta^4/\rho\sigma^3$. In our simulations, bubbles are assumed to be spherical at all times. In our experiments conducted in glycerine–water mixtures, Eo was 0.3–0.4; Ca was less than 0.01; We was 0.04–0.2; and Mo was 10^{-8}–10^{-5}. The maximum aspect ratio of the bubbles in our experiments was 1.1, and it occurred at the highest Reynolds number. As $We > Ca$, this deformation was primarily due to the inertia of the relative motion ρU_r^2 and was not induced by the shear. Because the values of these non-dimensional numbers are far below the range in which deformation has been observed to influence the lift force (Sankaranarayanan & Sundaresan 2002; Tomiyama *et al.* 2002; Bunner & Tryggvason 2003; Van Nierop *et al.* 2007), we can focus on spherical bubbles and characterize C_L^* as a function of Re, Sr and ϕ.

In order to characterize the dependence of C_L^* on ϕ, one needs to construct a shear flow in a non-dilute suspension in which each bubble interacts with other bubbles hydrodynamically. In such a suspension, as the distribution of pressure and viscous stress on the surface of a bubble would be influenced by bubble–bubble interaction, the lift force would be different from that on an isolated bubble. The first evidence that C_L^* depends on the volume fraction in a non-dilute suspension comes from Sankaranarayanan & Sundaresan (2002), who simulated the rise of a single three-dimensional bubble in a cubic computational domain with imposed shear using the two-component lattice Boltzmann method. The shear flow was generated by modifying the fluid molecular velocity distributions near the y-boundaries such that the fluid velocity satisfied $\boldsymbol{u} = \boldsymbol{e}_x\alpha y + \boldsymbol{u}'$, and $\boldsymbol{u}'$ was a function that was periodic in all three directions. As they characterized the lift force as a function of Eo, Mo and α, they found that for a spherical bubble ($Eo = 0.2$, $Mo = 10^{-10}$, $Re \sim 200$), the lift force coefficient was about 8 % higher than the theoretical value of 1/2 (Auton 1987) when the volume fraction occupied by the bubble in the computational domain was $\phi = 0.08$. The lift force coefficient then decreased with increasing domain size and approached 1/2 as $\phi \to 0$. This volume fraction dependence of the lift force is thus the result of the hydrodynamic interaction between the bubble and its periodic images.

In this paper, we will study the manner in which hydrodynamic interactions among bubbles affect the lift force in a disordered, freely evolving suspension, a situation that more faithfully mirrors physical experiments than the periodic array of Sankaranarayanan & Sundaresan (2002). Instead of using a forced shearing motion, our shear flow is established naturally and gradually in a slightly inclined bubble channel, where the cross-stream buoyancy force creates layers of excess and depleted bubble concentration near the upper and lower walls, and the resultant streamwise buoyancy force difference drives a shear flow. Our numerical data show that under certain conditions the shear flow in the middle of the inclined channel is nearly viscometric, and the force balance in the lateral direction only involves the

cross-stream buoyancy and the lift force, allowing the latter to be determined as a function of Re, Sr and ϕ. The complementary experimental study presented at the end of this paper confirms the existence of a viscometric shear-flow region in the middle of an inclined channel and shows qualitative agreement with the simulations.

This paper is organized as follows: In § 2, we describe the numerical method, define the inclined channel configuration and show that under the right conditions there exists a nearly viscometric shear flow in the middle of the channel. In § 3, we present C_L^* determined from the simulations, set up a simple x-momentum balance model and give the parameter range in which the viscometric flow conditions exist. In § 4, we present the experimental study of bubbly flows in inclined channels and compare the experimental results to the simulations. In the end, we discuss why C_L^* is enhanced by the hydrodynamic interaction among bubbles and conclude the paper.

2. Numerical method and the inclined channel configuration

Our numerical simulations are based on the lattice Boltzmann method developed by Ladd (1994*a*, *b*) for suspensions of spherical particles. This method has been improved over the years, and a review of it is available in Ladd & Verberg (2001). To account for the no-tangential-stress boundary condition on a clean bubble with negligible gas viscosity, we employed the first-order-accurate boundary rule based on nodal bounce back developed by Yin, Koch & Verberg (2006). To assist the readers to understand our numerical approach, we provide a brief description of the important aspects of the lattice Boltzmann method and the boundary rules. More detailed information can be found in Ladd (1994*a*, *b*), Ladd & Verberg (2001), Yin *et al.* (2006) and the references therein.

The lattice Boltzmann method is not a direct solver of the continuum Navier–Stokes equations. Rather, it solves the evolution of a fluid molecular-velocity distribution $n_i(\boldsymbol{r}, t) \equiv n(\boldsymbol{r}, \boldsymbol{c}_i, t)$ that describes the fraction of molecules at $\boldsymbol{r}$, with velocity $\boldsymbol{c}_i$, at time t. Both $\boldsymbol{r}$ and $\boldsymbol{c}_i$ are discrete variables: $\boldsymbol{r}$ takes on values from a three-dimensional cubic lattice with spacing Δx, and $\boldsymbol{c}_i$ is one of the 19 velocities that make the fluid molecules either stay at the current node ([000]) or move to the nearest ([001]) and the next nearest ([011]) lattice neighbours in one time step Δt. This discretization scheme is commonly referred to as the D3Q19 model. The macroscopic quantities, such as density ρ, momentum $\boldsymbol{j} = \rho \boldsymbol{u}$ and momentum flux (stress) $\boldsymbol{\Pi}$, are the zeroth first- and second-order moments of $n_i(\boldsymbol{r}, t)$:

$$\left.\begin{aligned} \rho &= \sum_i n_i, \\ \boldsymbol{j} &= \sum_i n_i \boldsymbol{c}_i, \\ \boldsymbol{\Pi} &= \sum_i n_i \boldsymbol{c}_i \boldsymbol{c}_i. \end{aligned}\right\} \tag{2.1}$$

The update of $n_i(\boldsymbol{r}, t)$ includes a collision step, where a linear collision operator Δ_i is applied to the distribution n_i to produce the *post-collision* distribution n_i^*

$$n_i^*(\boldsymbol{r}, t) = n_i(\boldsymbol{r}, t) + \Delta_i[n_i(\boldsymbol{r}, t)] \tag{2.2}$$

and a propagation step, where the fluid molecular populations at node $\boldsymbol{r}$ travel to the neighbouring nodes based on the velocity distribution $n_i^*(\boldsymbol{r}, t)$ just calculated:

$$n_i(\boldsymbol{r} + \boldsymbol{c}_i \Delta t, t + \Delta t) = n_i^*(\boldsymbol{r}, t). \tag{2.3}$$

Usually, n_i is split into an equilibrium part and a non-equilibrium part:

$$n_i = n_i^{eq} + n_i^{neq}. \tag{2.4}$$

The equilibrium distribution n_i^{eq} is given by

$$n_i^{eq} = a^{c_i}\left[\rho + \frac{\boldsymbol{j}\cdot\boldsymbol{c}_i}{c_s^2} + \frac{\rho\boldsymbol{u}\boldsymbol{u}:(\boldsymbol{c}_i\boldsymbol{c}_i - c_s^2\boldsymbol{I})}{2c_s^4}\right], \tag{2.5}$$

in which $\boldsymbol{I}$ is an identity matrix; c_s is the isothermal speed of sound in the lattice fluid, which equals $(1\sqrt{3})\Delta x/\Delta t$; and the weighting factors a^{c_i} describe the fraction of molecules moving in the direction of $\boldsymbol{c}_i$, the values of which are 1/3, 1/18 and 1/36, respectively, for the [000], [001] and [011] directions. When there is no fluid flow ($\boldsymbol{u}=0$), the sum of n_i^{eq} yields the static density of the lattice fluid ρ_0, which is taken to be 36 in this study.

The shear and bulk viscosities of the lattice fluid are incorporated in the collision operator Δ_i, which in this study involves two relaxation parameters (Ladd & Verberg 2001; d'Humières *et al.* 2002) and is of the following form:

$$\boldsymbol{\Pi}^{neq,*} = (1+\lambda)\overline{\boldsymbol{\Pi}^{neq}} + \frac{1}{3}(1+\lambda_B)(\boldsymbol{\Pi}^{neq}:\boldsymbol{I})\boldsymbol{I}. \tag{2.6}$$

Here $\boldsymbol{\Pi}^{neq} = \sum_i n_i^{neq}\boldsymbol{c}_i\boldsymbol{c}_i$ is the non-equilibrium stress; $\boldsymbol{\Pi}^{neq,*}$ is the post-collision non-equilibrium stress; and $\overline{\boldsymbol{\Pi}^{neq}}$ is the traceless part of $\boldsymbol{\Pi}^{neq}$. The relaxation parameters λ and λ_B are in the range $(-2, 0)$ and are related to the shear and bulk viscosities of the fluid by

$$\left.\begin{aligned} \eta &= -\rho c_s^2\Delta t\left(\frac{1}{\lambda}+\frac{1}{2}\right), \\ \eta_B &= -\frac{2}{3}\rho c_s^2\Delta t\left(\frac{1}{\lambda_B}+\frac{1}{2}\right). \end{aligned}\right\} \tag{2.7}$$

In this study, we adjusted λ and λ_B such that $\eta = 0.36$ and $\eta_B = 4.0$. With $\boldsymbol{\Pi}^{neq,*}$ determined, the post-collision velocity distribution n_i^* can be calculated from

$$n_i^* = a^{c_i}\left[\rho + \frac{\boldsymbol{j}\cdot\boldsymbol{c}_i}{c_s^2} + \frac{(\rho\boldsymbol{u}\boldsymbol{u} + \boldsymbol{\Pi}^{neq,*}):(\boldsymbol{c}_i\boldsymbol{c}_i - c_s^2\boldsymbol{I})}{2c_s^4}\right]. \tag{2.8}$$

This collision operator satisfies the local conservation of mass and momentum and recovers the Navier–Stokes equations on the macroscopic scale with a compressibility error of $O(M^2)$, where $M = |\boldsymbol{u}|/c_s$ is the Mach number. When the body force acting on the fluid is zero, (2.8) applies; if an external body force $\boldsymbol{f}$ is present, e.g. gravity, the evolution of n_i includes an extra term:

$$n_i^* = a^{c_i}\left[\rho + \frac{(\boldsymbol{j}+\boldsymbol{f}\Delta t)\cdot\boldsymbol{c}_i}{c_s^2} + \frac{(\rho\boldsymbol{u}\boldsymbol{u} + \boldsymbol{\Pi}^{neq,*}):(\boldsymbol{c}_i\boldsymbol{c}_i - c_s^2\boldsymbol{I})}{2c_s^4}\right]. \tag{2.9}$$

In two-phase flows, when a fluid molecular population n_i is directed from a fluid node to a non-fluid node, it needs to be modified and returned to the fluid node to conserve mass and recover the specific boundary condition between the two phases. The commonly used linked-bounce-back rule,

$$n_{i'}(\boldsymbol{r}, t+\Delta t) = n_i^*(\boldsymbol{r}, t) - \frac{2\rho a^{c_i}\boldsymbol{c}_i\cdot\boldsymbol{u}_b(\boldsymbol{r}_b, t)}{c_s^2}, \tag{2.10}$$

recovers the no-slip boundary condition at a boundary node $\boldsymbol{r}_b = \boldsymbol{r} + \frac{1}{2}\boldsymbol{c}_i \Delta t$ halfway between the fluid node at $\boldsymbol{r}$ and the solid node at $\boldsymbol{r} + \boldsymbol{c}_i \Delta t$. In (2.10), $n_{i'}$ is the population returned to the fluid node with a velocity $\boldsymbol{c}_{i'}$ in the opposite direction to $\boldsymbol{c}_i$, and $\boldsymbol{u}_b$ is the velocity of the solid at the boundary node $\boldsymbol{r}_b$. In order to recover the no-tangential-stress boundary condition on a gas–liquid interface

$$\left.\begin{aligned} &\boldsymbol{n}\cdot\boldsymbol{u} = \boldsymbol{n}\cdot\boldsymbol{u}_b, \\ &\boldsymbol{n}\cdot\boldsymbol{\sigma}\cdot(\boldsymbol{I}-\boldsymbol{nn}) = 0, \end{aligned}\right\} \tag{2.11}$$

on a boundary node $\boldsymbol{r}_b$ lying halfway between a fluid node and a non-fluid node, with $\boldsymbol{n}$ representing the surface normal and $\boldsymbol{\sigma}$ the fluid stress at $\boldsymbol{r}_b$, Yin *et al.* (2006) developed a new linked-bounce-back rule

$$\begin{aligned} n_{i'}(\boldsymbol{r}, t+\Delta t) = n_i^*(\boldsymbol{r}, t) &- \frac{2a^{c_i}}{c_s^2}\left[\rho \boldsymbol{c}_i\cdot\boldsymbol{nn}\cdot\boldsymbol{u}_b(\boldsymbol{r}_b, t) + \boldsymbol{c}_i\cdot(\boldsymbol{I}-\boldsymbol{nn})\cdot j(\boldsymbol{r}, t)\right] \\ &- \frac{\lambda a^{c_i}}{2c_s^4}\boldsymbol{c}_i\cdot(\boldsymbol{I}-\boldsymbol{nn})\cdot\overline{\boldsymbol{\Pi}^{neq}}(\boldsymbol{r}, t)\cdot(\boldsymbol{I}-\boldsymbol{nn})\cdot\boldsymbol{c}_i. \end{aligned} \tag{2.12}$$

It was shown that this boundary rule can accurately simulate steady and unsteady gas–liquid flows with flat or curved tangential-stress-free interfaces in the Reynolds number range $0 < Re < 30$ with first-order accuracy in the spatial discretization. When applied to a spherical bubble, the accuracy can be improved to approximately second order by introducing a hydrodynamic correction to the radius of the bubble, which can be obtained from calibration runs that compare the Stokes drag of a spherical bubble in a periodic array to the analytical solutions (Sangani & Acrivos 1983).

In our simulations, the dynamics of the fluid phase was solved by the lattice Boltzmann method just described, and the motion of the bubbles was determined from Newton's equations of motion using the net fluid–bubble interactive force obtained from a surface integral of fluid stresses, the buoyancy force and a small bubble mass based on a gas-to-fluid density ratio of $\rho_g/\rho = 0.001$. The buoyancy force, in particular, was specified by the Archimedes number of the bubbles

$$Ar = \frac{\rho^2|\boldsymbol{g}|d^3}{\eta^2}, \tag{2.13}$$

which is a defining dimensionless parameter of our simulations. We chose the magnitudes of $\boldsymbol{g}$ such that the Archimedes numbers were 87.8, 198 and 451. According to the single-bubble simulations in Yin *et al.* (2006), these values of Ar yield terminal Reynolds numbers of approximately 5.4, 10 and 20. The Reynolds numbers based on the relative velocities U_r were in the range 4–16 and were only slightly higher than the hindered rise velocities found in unbound suspensions with periodic boundary conditions of the same Ar and volume fraction (see table 1). Thus, a slight inclination does not seem to have a significant influence on the mean rise velocity of bubbles. Legendre & Magnaudet (1998) found that a weak imposed shear ($Sr < 0.5$) does not affect the drag coefficient on an isolated bubble when Re is in the range 300–500. Our observations suggest that the same is true in suspensions with more moderate Reynolds numbers.

In dynamic simulations of solid particle suspensions, explicit lubrication corrections are generally needed to capture the strong lubrication forces (e.g. Sangani & Mo 1994; Nguyen & Ladd 2002) that arise in the narrow gap between a close pair of solid particles. The lubrication interaction between a pair of spherical bubbles is generally

Ar	*Re* (inclined)		*Re* (vertical)	
	$\phi_0 = 0.05$	$\phi_0 = 0.1$	$\phi_0 = 0.05$	$\phi_0 = 0.1$
87.8	4.4–4.6	3.8–4	4.3	3.6
198	8.4–8.5	7.4–7.5	(not tested)	(not tested)
451	16.1–16.2	14.3–14.4	16.0	14.2

TABLE 1. The Reynolds numbers based on U_r in inclined channels compared to those in unbound suspensions [characterized in Yin (2007)]. The values of *Re* in inclined channels are specified in a range because there is some variation of *Re* with the inclination angle θ, the detail of which can be found in Table 2 and Table 3; ϕ_0 stands for the average volume fraction in the suspension.

weak (Kim & Karrila 2005), however, and therefore we did not apply explicit lubrication corrections to the bubbles. When bubbles collided with each other, elastic collisions were assumed, consistent with the observations made in bubble suspensions stabilized by added electrolytes (Tsao & Koch 1994).

Most of the simulations were performed with an effective bubble diameter of $6.7\Delta x$, a resolution that was found be adequate in the various test cases involving bubble–bubble hydrodynamic interactions and steady/unsteady motions of bubbles examined by Yin *et al.* (2006). In addition, we verified the accuracy of the grid resolution in our application by confirming that comparable results were obtained for $d = 12.1\Delta x$ (cf. figure 2; table 2; table 3).

Our simulations were conducted in rectangular computational domains with periodic boundary conditions applied to the x and z boundaries and a pair of solid walls applied to the y boundaries. The ratio of the gap between the solid walls to the bubble diameter was chosen to be $L_y/d = 14$ to match the y-dimension of our experimental channel. The periodic length in the x and z directions was $L_x = L_z = 14d$. Simulations with twice the value of L_x or L_z showed that the periodic boundary conditions did not influence the results. The gravitational acceleration $\boldsymbol{g}$ was oriented in the x–y plane, with a small angle θ relative to the x-axis to simulate the effect of the inclination, as shown in figure 1.

Simulations were initiated with N bubbles randomly distributed in the domain with zero velocity. The average volume fraction ϕ_0, the other defining dimensionless simulation parameter in this study, is related to N by $\phi_0 = N\pi d^3/6L_xL_yL_z$. As the buoyancy force $\rho|\boldsymbol{g}|\pi d^3/6$ assigned to the bubbles had a small angle relative to the x-axis, bubbles would gradually migrate towards the upper wall at $y = 14d$ while rising in the x-direction, leading to a more buoyant suspension near the upper wall and a less buoyant one near the bottom wall. The asymmetric distribution of buoyancy force per unit volume of suspension then exerts a moment on the bulk suspension and generates a shear flow that gradually stops the lateral migration of bubbles through the lift force. The progress of the suspension towards the steady state was checked by monitoring the average y-position of all bubbles. Typically, the average y-position of bubbles stabilizes after a dimensionless time $t^* = tU_r/d$ of about 100–200. Thereafter, a steady state that features a bubble-rich layer near the upper wall, a depleted layer that is essentially free of bubbles near the bottom wall and a viscometric bulk suspension, where the velocity gradient α (< 0), volume fraction ϕ and the relative velocity U_r all become nearly independent of y, is developed. Then, we conducted time averaging over 400 to 800 t^* to obtain statistically accurate steady-state volume fraction and velocity profiles.

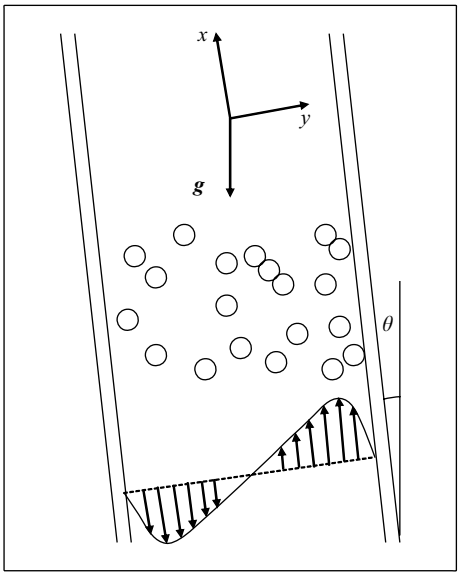

FIGURE 1. Schematic of the inclined channel configuration.

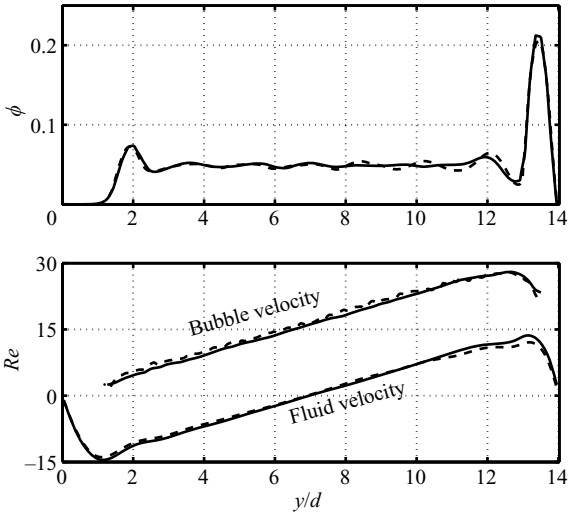

FIGURE 2. The volume fraction and the bubble and fluid velocity profiles in an inclined channel, where $Ar = 451$, $\phi_0 = 0.05$ and $\theta = 2^\circ$. The Reynolds number based on the relative velocity between the bubbles and the fluid was 16.1. The top figure shows the volume fraction profile, and the bottom figure shows the bubble and the fluid velocity profiles. The solid lines were obtained using the lattice resolution of $d = 6.7\,\Delta x$; the broken lines were obtained using a higher resolution of $d = 12.1\,\Delta x$, showing the results were independent of lattice resolution.

Figure 2 shows a sample of the steady-state volume fraction and velocity profiles obtained for $Ar = 451$ and $\phi_0 = 0.05$ and in a channel with 2° inclination angle. The volume fraction profile reveals a bubble-rich layer about $1.4\,d$ thick near the top wall and a depleted layer of a similar thickness near the bottom wall; the small peak near the depleted region is due to the sign change of the lift force in the region in which the fluid velocity had to turn to satisfy the no-slip wall boundary condition; the

volume fraction in the bulk suspension is fairly constant, and so are the inter-phase slip velocity and the bubble and fluid velocity gradients. In the next section of this paper, we will examine more of these simulations and extract the lift force from the force balance in the bulk suspension. We will also introduce a simple analytical model for bubbly flows in slightly inclined channels and explore the parameter space (Re, θ and ϕ_0) to find the regime where a viscometric steady state such as that illustrated in figure 2 exists.

3. Determining the lift coefficient in a sheared suspension

In most bubbly flows, the motion of bubbles is controlled by a variety of factors including drag, buoyancy, lift, added mass, history effect and bubble-phase stresses. As we are interested in steady-state properties in an inclined channel and as bubbles in the bulk no longer migrate to the upper wall after the steady state is established, added mass, history force and drag can be excluded from the force balance in the lateral direction. This leaves the bubble-phase stresses along with lift and buoyancy forces as possible influences on the bubbles in the bulk suspension.

Bubble-phase stresses control the kinetic transport of bubbles in a suspension and can be attributed to bubble velocity fluctuations, collision and hydrodynamic interactions in shear flow and free rise (Sangani & Didwania 1993; Bulthuis, Prosperetti & Sangani 1995; Kang *et al.* 1997; Spelt & Sangani 1998). In our simulations, bubble–bubble direct collisions were rare and took place only within the bubble-rich layer. Still, a gradient in the bubble-phase stress can develop due to spatial variations in bubble concentration, bubble velocity fluctuation, mean shear rate or average slip velocity, and bubbles will be driven towards regions with lower volume fraction, lower velocity fluctuation, lower shear or higher slip velocity. Interestingly, all of these variables were nearly constant in the bulk suspension at the steady state. Figure 2 indicates that there are no variations in the volume fraction, the average slip velocity and the velocity gradient in the bulk suspension; in addition, figure 3 shows that the velocity variance of the bubbles $\langle U_i' U_j' \rangle / U_r^2$ is also nearly invariant in the bulk. These results suggest that the shear flow of the bulk suspension is highly viscometric; the effect of bubble-phase stress gradient can be excluded; and the cross-stream force balance only involves the lift force and the buoyancy component normal to the walls.

The simple viscometric flow with a balance of lift and buoyancy observed in our simulations may be contrasted with the experimental study of Zenit *et al.* (2004), involving bubbles with higher Reynolds numbers in the range $300 \sim 400$. In that study the volume fraction varied significantly across the gap, and one of its conditions was that the cross-stream momentum balance must include bubble-phase stress gradients as well as buoyancy and lift. The larger fluctuating velocities in the high Reynolds number study may be one factor accounting for this difference.

From the balance between the buoyancy and the lift, we can compute the lift force coefficient in a bubble suspension using the following equation:

$$C_L^* = \frac{-g_y}{\alpha U_r} = \frac{Ar \sin\theta}{Re^2 Sr}, \tag{3.1}$$

where g_y is a specified quantity; and α and U_r were obtained from the steady-state velocity profiles in the bulk ($4 < y/d < 10$). In table 2 and table 3, we list the values of C_L^* obtained from simulations with $\phi_0 = 0.05$ and 0.1, respectively. It is clear that C_L^* for a freely evolving suspension is higher than the corresponding C_L under isolated

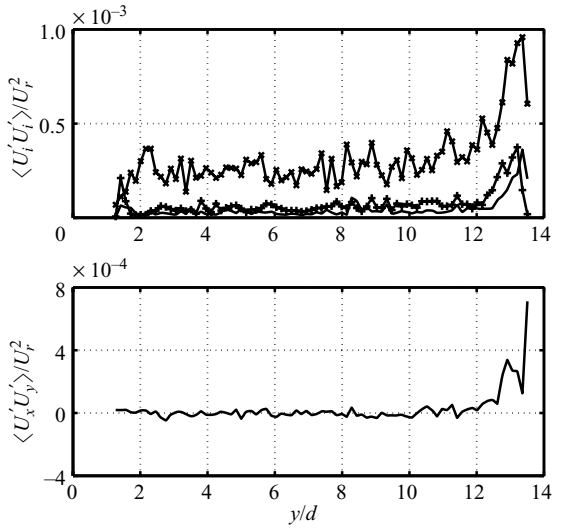

FIGURE 3. The bubble velocity variances $\langle U_i' U_j' \rangle / U_r^2$ in the flow described in the caption of figure 2. In the top figure, the line marked with '×' represents $\langle U_x' U_x' \rangle / U_r^2$, the line marked with '+' $\langle U_y' U_y' \rangle / U_r^2$ and the line with no mark $\langle U_z' U_z' \rangle / U_r^2$. In the bottom figure, the solid line represents $\langle U_x' U_y' \rangle / U_r^2$. Being nearly zero across the entire channel, $\langle U_y' U_z' \rangle / U_r^2$ and $\langle U_z' U_x' \rangle / U_r^2$ are not shown.

Ar	θ	Re	Sr	C_L^*	C_L	$C_L^*/C_L - 1$
87.8	2°	4.36	0.20	0.80	0.33	1.4
198	2°	8.44	0.17	0.56	0.33	0.71
	4°	8.51	0.38	0.50	0.33	0.51
451	2°	16.1 (16.5)	0.14 (0.14)	0.42 (0.41)	0.36 (0.36)	0.16 (0.14)
	4°	16.2	0.29	0.42	0.36	0.16

TABLE 2. The values of bubble Reynolds number and Sr in the bulk suspension and the corresponding lift force coefficient C_L^* at different inclination angles. The average volume fraction of the suspension is $\phi_0 = 0.05$. It is clear from this table that (1) the lift force coefficient C_L^* in a sheared suspension is larger than C_L for isolated bubbles; (2) the ratio C_L^*/C_L decreases with increase in Re. The numbers in parentheses were obtained from simulations with $d = 12.1\Delta x$.

condition, consist with the earlier result of Sankaranarayanan & Sundaresan (2002) obtained for a periodic array of bubbles. C_L^*/C_L is not exactly linear in ϕ_0. However, if we were to use $C_L^*/C_L = 1 + A\phi_0$ to fit the dependence of C_L^* on ϕ_0, the value of A would decrease with increasing Reynolds number from 8–15 (depending on the inclination angle θ) when $Re \sim 4$ to about 2 if Re were in the range 14–16. The reduction in A with increasing Re can be related to the fact that the range and strength of the hydrodynamic interaction generally decrease with increasing Reynolds number. In Sankaranarayanan & Sundaresan's periodic suspensions, A was about 1 when $Re \sim 200$. Therefore, we may infer that A would continue to decrease with increasing Re over a wide range of values.

Ar	θ	*Re*	*Sr*	C_L^*	C_L	$C_L^*/C_L - 1$
	2°	3.78	0.20	1.08	0.34	2.2
87.8	4°	3.92	0.40	1.00	0.37	1.7
	6°	3.95	0.64	0.93	0.40	1.3
	2°	7.37	0.18	0.72	0.32	1.2
198	4°	7.44 (7.63)	0.34 (0.31)	0.72 (0.76)	0.33 (0.33)	1.2 (1.3)
	6°	7.50	0.54	0.68	0.34	1.0
	2°	14.3	0.16	0.48	0.35	0.36
451	4°	14.4	0.30	0.51	0.35	0.45
	6°	14.4 (15.0)	0.44 (0.41)	0.51 (0.50)	0.35 (0.35)	0.46 (0.43)

TABLE 3. The values of bubble Reynolds number and *Sr* in the bulk suspension and the corresponding lift force coefficient C_L^* at different inclination angles. The average volume fraction of the suspension is $\phi_0 = 0.10$. The numbers in parentheses were obtained from simulations with $d = 12.1\Delta x$.

We can use a simple x-momentum balance for the bubble suspension to calculate the volume fraction profile needed to drive a given shear flow in an inclined channel. As the bubbly flow in the channel is unidirectional, the fluid motion is governed by the x-momentum equation

$$\eta \frac{\mathrm{d}^2 u_x}{\mathrm{d}y^2} - \frac{\mathrm{d}p}{\mathrm{d}x} + \phi(y)\rho g_x = 0. \tag{3.2}$$

In (3.2), $\phi(y)\rho g_x$ ($g_x < 0$) represents the body force acting on the suspension due to the presence of bubbles, and $\mathrm{d}p/\mathrm{d}x$ is the reverse pressure gradient that keeps the average fluid velocity zero. At low Reynolds numbers, Taylor (1932) showed that the shear viscosity of a dilute bubble suspension is $(1 + \phi)\eta$, which is not much different from η for the bulk volume fractions studied in this paper. The fluctuating motion of the bubbles can also create an effective viscosity at higher Reynolds numbers. However, the values of the bubble velocity variance such as those in figure 3 indicate that this contribution to the viscosity will be small. Thus, for simplicity, we approximated the shear viscosity of the bubble suspension as equal to the fluid viscosity.

Since the reverse pressure gradient must balance the total buoyancy force from the bubbles, and $\mathrm{d}p/\mathrm{d}x = -\phi_0 \rho g_x$, we can rewrite (3.2) as

$$\eta \frac{\mathrm{d}^2 u_x}{\mathrm{d}y^2} + [\phi(y) - \phi_0]\rho g_x = 0, \tag{3.3}$$

where ϕ_0 is the average bubble concentration in the entire suspension. This equation allows us to determine the fluid velocity profile $u_x(y)$ for any given volume fraction profile $\phi(y)$.

Because the volume fraction profiles obtained from simulations (e.g. figure 2) exhibit a constant-volume-fraction bulk region sandwiched between thin layers that are bubble-rich and depleted in bubble concentration at the upper and lower walls, it is reasonable to approximate $\phi(y)$ in a slightly inclined channel using a profile with two step changes:

$$\phi(y) = \begin{cases} 0, & 0 < y < H_1, \\ \phi_0, & H_1 < y < L_y - H_2, \\ (1 + H_1/H_2)\,\phi_0, & L_y - H_2 < y < L_y, \end{cases} \tag{3.4}$$

where H_1 and H_2 represent, respectively, the widths of the depleted and bubble-rich layers. This profile satisfies the constraint that $\int_0^{L_y} \phi \, \mathrm{d}y = \phi_0 L_y$. Using this model, the determination of the volume fraction profile is reduced to determining the widths, H_1 and H_2, of the two layers. In the subsequent analysis we will find the widths H_i required to produce a given shear rate α. In turn, α is determined by the constraint that the lift and buoyancy forces balance in the cross-stream direction.

When (3.4) is substituted into (3.3), it is clear that the fluid layers near the walls are subjected to equal and opposite body forces, generating a moment on the body-force-free bulk suspension and producing a linear velocity profile allowing the determination of the lift force. As the body forces are independent of y within each layer, the profiles of $u_x(y)$ must be quadratic in the wall layers. Thus, the velocity profile takes the form

$$u_x = \begin{cases} A_1 y^2 + B_1 y + C_1, & 0 < y < H_1, \\ \alpha y + C_2, & H_1 < y < L_y - H_2, \\ A_3 y^2 + B_3 y + C_3, & L_y - H_2 < y < L_y, \end{cases} \tag{3.5}$$

where A_i, B_i, C_i are undetermined, and $\alpha = \mathrm{d}u_x/\mathrm{d}y$ is the velocity gradient in the bulk that equals $-g_y/U_r C_L^*$. Together with H_1 and H_2, the total number of unknowns in (3.5) is nine. The no-slip boundary condition at $y = 0$ and $y = L_y$ and the continuity of velocities and stresses at $y = H_1$ and $y = L_y - H_2$ provide six equations; the momentum equations in the wall layers (3.3) and the constraint of no net fluid flow $\int_0^{L_y} u_x \mathrm{d}y = 0$ provide three equations. The equations are thus closed, and the thickness of the wall layers and the constants in the fluid velocity profile can be determined for a given shear rate. In figure 4, we show the fluid velocity and volume fraction profiles obtained from the x-momentum balance (3.3) for cases with different Ar, ϕ_0 and θ. It can be observed that the liquid velocity profiles are very close to those found in the simulations. The widths of the wall layers are also in good agreement with the simulated volume fraction profiles. This comparison shows that the relation between the volume fraction profile and the given viscometric shear flow in a slightly inclined channel is indeed governed by a simple x-momentum balance.

From the volume fraction profiles, we can calculate the first moment of the volume fraction distribution, defined as

$$M = \frac{4}{\phi_0 L_y^2} \int_0^{L_y} [\phi(y) - \phi_0] \left(y - \frac{L_y}{2} \right) \mathrm{d}y. \tag{3.6}$$

It is a measure of the buoyancy difference that produces the shearing motion of the bulk suspension. M defined in (3.6) has two important limits: if $\phi = \phi_0$ everywhere in the channel, $M = 0$; on the other hand, if $\phi = 2\phi_0$ in the upper half of the channel and if $\phi = 0$ in the lower half, $M = 1$. We calculated the values of M using (3.4) and (3.5), the x-momentum balance equations, and list them in table 4. In the same table, we also include the moments obtained from simulation profiles. The moments obtained from the x-momentum balance and those from simulations showed the same qualitative trend of M increasing with increasing θ and with decreasing Re and ϕ. The quantitative differences between the model predictions and the simulations, which were the smallest at the lowest inclination angle of 2° and increased with increasing θ, suggest that the flows in channels with higher inclination angles become less viscometric. Of course, the assumed shape of the volume fraction profile and

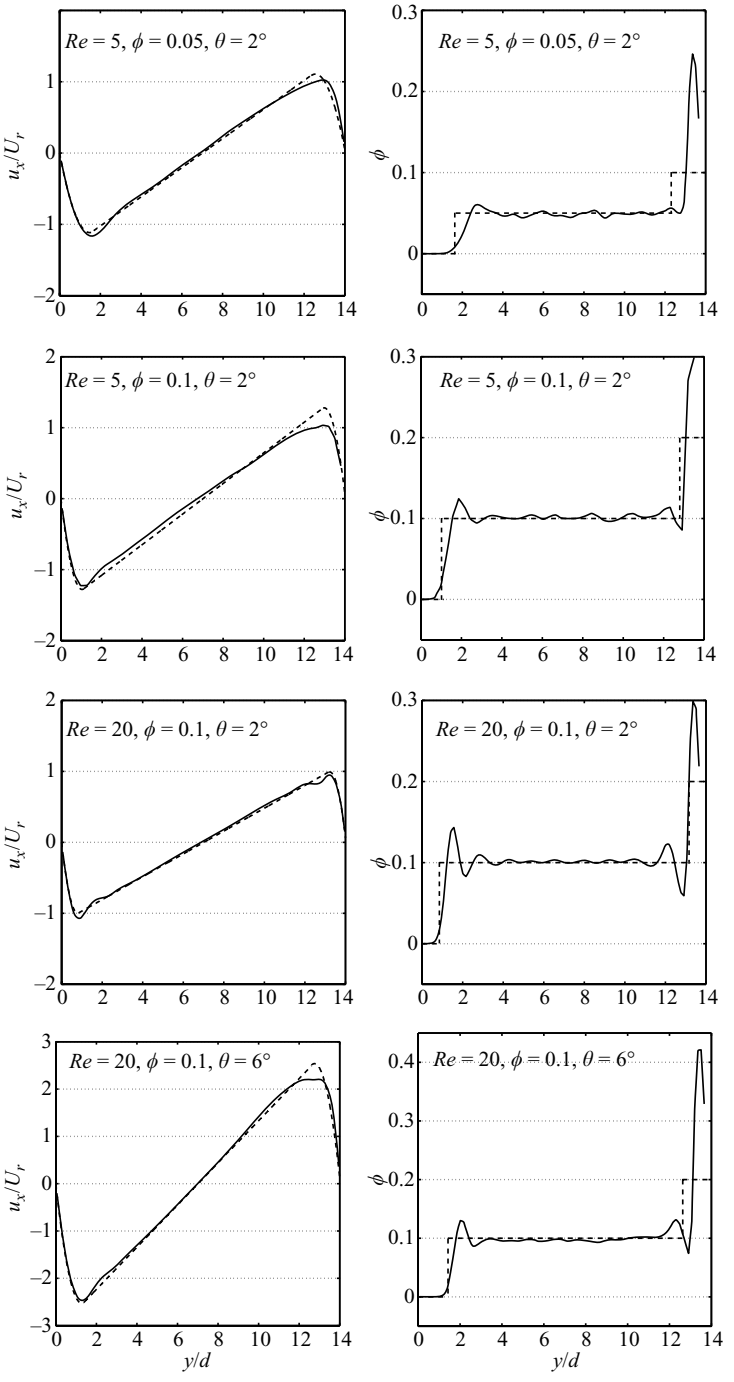

FIGURE 4. Fluid velocity profiles (left) and bubble volume fraction profiles (right) derived from (3.4) and (3.5) (broken lines) compared to the profiles obtained from the simulations (solid lines).

Ar	ϕ	$\theta = 2^\circ$	$\theta = 4^\circ$	$\theta = 6^\circ$
87.8	0.05	0.494/0.421		
	0.1	0.271/0.288	0.488/0.400	0.618/0.489
198	0.05	0.434/0.368	0.723/0.518	
	0.1	0.244/0.255	0.383/0.349	0.520/0.426
451	0.05	0.365/0.314	0.549/0.425	
	0.1	0.215/0.226	0.316/0.302	0.416/0.363

TABLE 4. The first moment of the volume fraction distribution in an inclined channel. The numbers before the slash are the moments from simulations; the numbers after the slash are from solving the x-momentum balance model equations (3.4) and (3.5).

the assumption that the shear viscosity was unaffected by the bubbles may also have contributed to these differences.

In order to determine the border of the viscometric shear flow regime in the (Ar, ϕ_0, θ) parameter space, for each combination of Ar and ϕ_0 we gradually increased the inclination angle θ until $|\phi_0 - \phi|/\phi_0$ exceeded 0.1 in the middle of the channel ($4 < y/d < 10$). We took $|\phi_0 - \phi|/\phi_0 < 0.1$ as the criterion to define the border of the viscometric flow regime, because the reduction in the average volume fraction in the bulk is the most sensitive measure of the system's departure from the ideal, viscometric flow state as described by the one-dimensional analytical model. The one-dimensional model requires $\phi = \phi_0$ in the bulk suspension, so that the bulk suspension is body force–free, and the velocity profile is linear. Figures 5–7 show that both the width of the region of constant volume fraction and the average volume fraction in this region decrease with increasing θ. The reduction in the linearity of the velocity profiles in the bulk ($4 < y/d < 10$), however, is not as obvious, even though the analytical model predicts that this would occur as soon as ϕ becomes less than ϕ_0.

Figures 5–7 indicate that the viscometric flow will break down when the inclination angle becomes too large: it becomes difficult then for the bubble-rich and the depletion layers to generate sufficient shear rate and lift force to match the cross-stream buoyancy. As illustrated in figure 8(a), systems with high inclination angles generally reach steady states with non-viscometric velocity and volume fraction profiles, and the effect of bubble-phase stress gradients must be considered in the lateral force balance. Figures 5–7 also suggest that the range of θ leading to viscometric flows increases with increasing Re and ϕ_0. The dependence on the Reynolds number may be understood by noting that the lift force is an inertial effect; a lower Re leads to a weaker lift force that eventually becomes insufficient to balance the cross-stream buoyancy. In fact, at $Re = 0.1$, the lift force is negligible, and we did not observe a viscometric flow even at $\theta = 2^\circ$ (cf. figure 8(b) for illustrations of steady-state velocity and volume fraction profiles). The dependence of the size of the viscometric flow region on ϕ_0, on the other hand, is related to the available buoyancy force per unit volume of suspension. In suspensions with a higher ϕ_0, as there is more buoyancy per unit volume, the streamwise buoyancy force moment required to drive the necessary shearing motion can be produced with a smaller relative variation of the volume fraction, and this allows the range of viscometric flows to extend to higher θ than in suspensions with a lower ϕ_0.

Figure 9 offers a direct view of the distribution of viscometric flows on a Re–θ map. The borders of the viscometric shear flow region, as we mentioned, are defined based

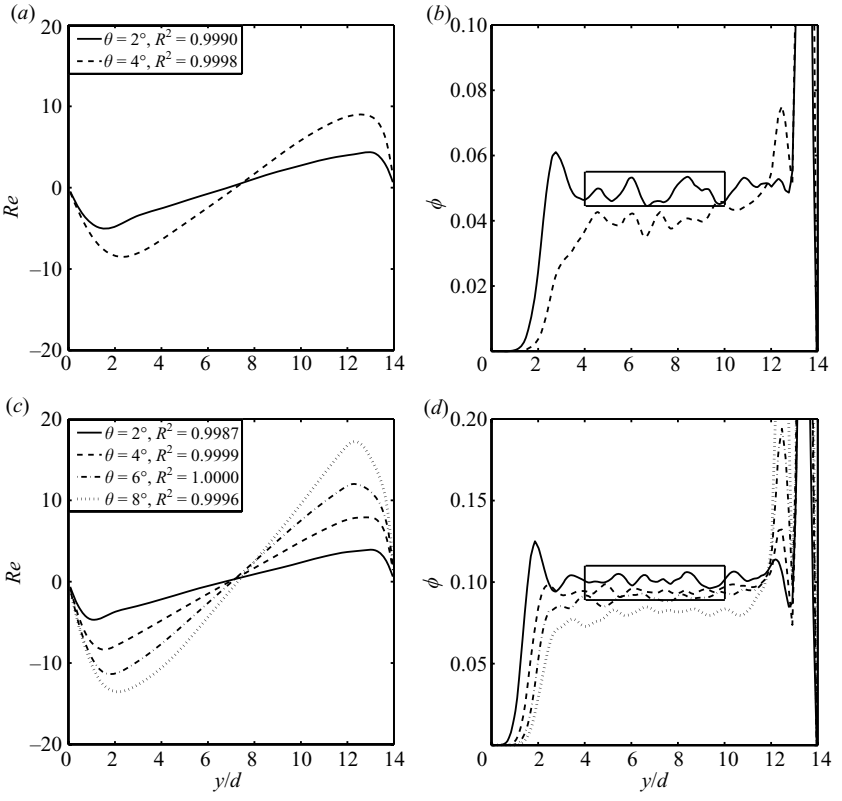

FIGURE 5. Changes in the fluid velocity profile (left) and in the volume fraction profile (right) with increasing inclination angle. The Archimedes number of the bubbles is 87.8, which corresponds to a bubble Reynolds number of 5.4 (based on the terminal velocity). The volume fraction ϕ_0 is 0.05 for (*a*) and (*b*) and 0.1 for (*c*) and (*d*). Lines of different styles represent profiles obtained at different inclination angles, see legends in (*a*) and (*c*). The R^2 values indicate the quality of linearity of the fluid velocity profile in the region $4 < y/\mathrm{d} < 10$. The criterion for the determination of the bound of the viscometric flow region, $|\phi_0 - \phi|/\phi_0 < 0.1$, is shown in (*b*) and (*d*) as rectangular boxes.

on the criterion $|\phi_0 - \phi|/\phi_0 < 0.1$ in the bulk $4 < y/d < 10$. Note that *Re* in figure 9 is defined based on the terminal velocity of bubbles, so it is independent of ϕ. Clearly, the range of acceptable θ expands with increasing *Re*, and the viscometric shear flow region becomes much larger when the average volume fraction of the suspension is increased from $\phi_0 = 0.05$ to $\phi_0 = 0.1$.

4. Experiments on bubbly flows in inclined channels

In this section, we present measurements of the bubble volume fraction and velocity profiles in a channel inclined 2° from the vertical direction. The average bubble concentration in the channel was $\phi = 0.1$. By adding glycerine (ACS grade) to water (HPLC grade), we increased the viscosity of the fluid phase and reduced the bubble Reynolds numbers to a range of 2–16, which is comparable to that explored in the simulations. Glycerine–water mixtures have been used by Maxworthy *et al.* (1996) to study the rise of isolated bubbles in viscous fluids. Although the surface tension of a glycerine–water mixture varies somewhat with composition, we are aware

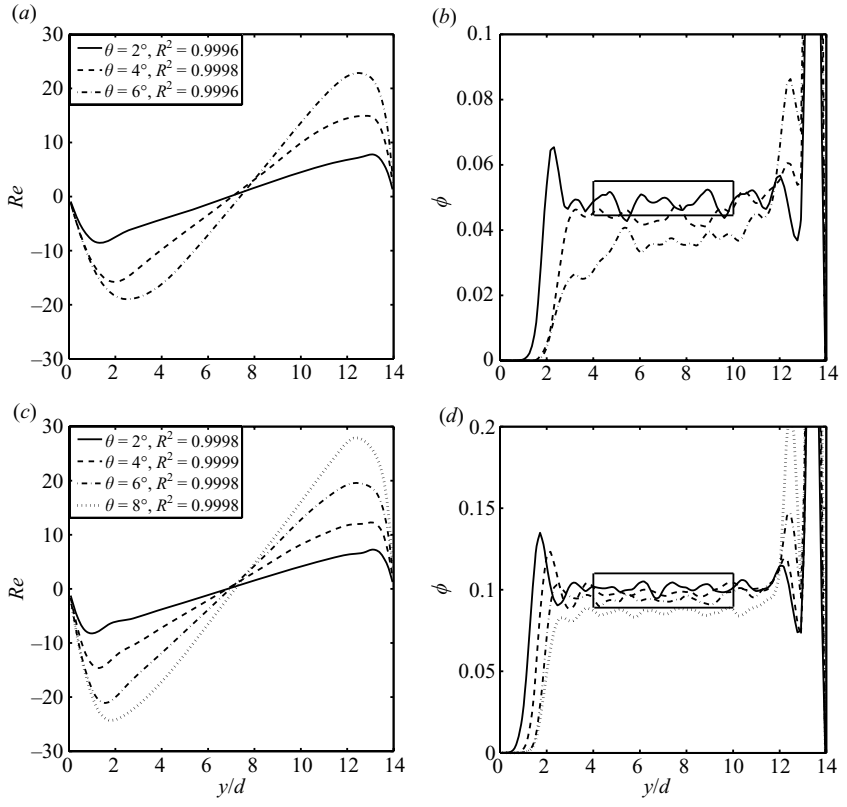

FIGURE 6. Similar to figure 5 except that the Archimedes number of the bubbles is 198, and the Reynolds number is 10 (based on the terminal velocity).

of no evidence of such a mixture exhibiting Marangoni effects. Indeed favourable comparisons between experiments and computations that neglect Marangoni stresses have been obtained even for jet break-up flows which exhibit considerable surface dilation (Chen, Notz & Basaran 2002).

An important difference between our experiments and those of Maxworthy *et al.* (1996) is that we also dissolved $0.3\,\mathrm{mol\,l^{-1}}$ magnesium sulphate in the fluid phase. The role of the magnesium sulphate, on one hand, is to suppress bubble coalescence and maintain a narrow bubble size distribution (Lessard & Zieminski 1971; Zenit, Koch & Sangani 2001; Zenit *et al.* 2004) without changing the zero-tangential-stress boundary condition. The surface tension of an aqueous solution is very insensitive to the concentration of electrolyte (Weissenborn & Pugh 1996). On the other hand, magnesium sulphate increases the electric conductivity of the fluid phase, allowing electric impedance probes (Zenit, Koch & Sangani 2003) to be used to detect passing bubbles.

In any experiment involving bubble suspensions, it is important to ensure the cleanness of the liquid, as surface contaminants can lead to Marangoni stresses and modify the no-tangential-stress boundary condition on the gas–liquid interface. Measurement of the mean rise velocity in our bubble suspension suggests the absence of surface contaminants. Our earlier numerical simulations indicate that spherical bubbles with $Ar = 451$ would rise with a Reynolds number of 14 when the bubble volume fraction is 0.1 (cf. table 1). In the experiments, bubbles with $Ar = 414$ were

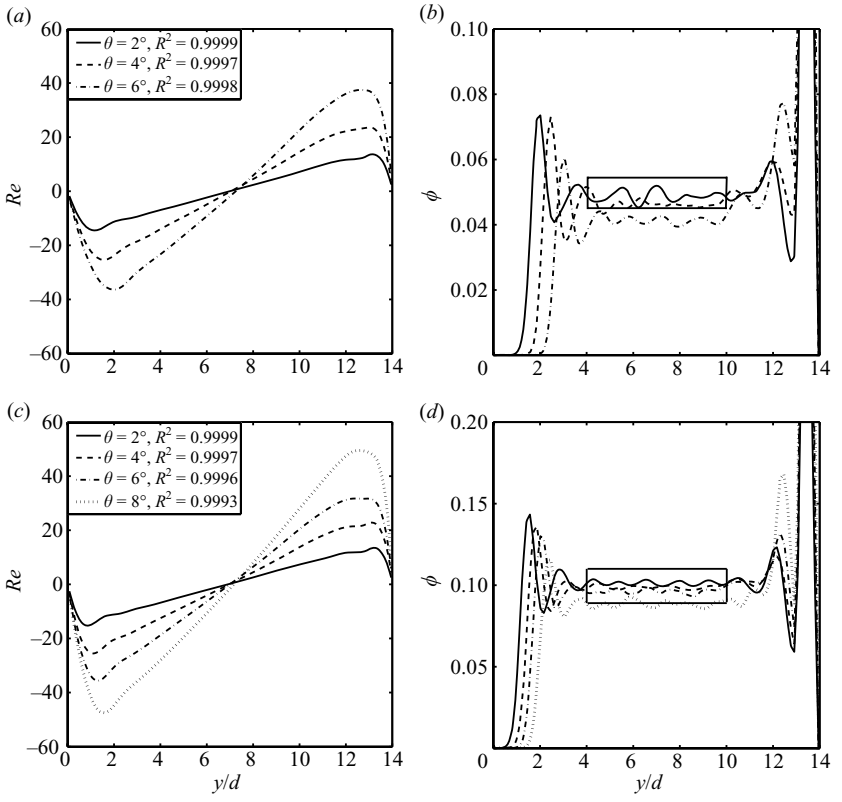

FIGURE 7. Similar to figure 5 except that the Archimedes number of the bubbles is 451, and the Reynolds number is 20 (based on the terminal velocity).

observed to rise with the Reynolds number of 12 when the volume fraction was 0.1 (cf. table 5). In view of the facts that a lower *Ar* leads to a lower *Re*, and a slightly deformable bubble generally rises a bit slower than a spherical bubble, it is reasonable to believe that the effect of surface contamination is small, and the no-tangential-stress boundary condition is well preserved in our system. Generally speaking, experiments involving bubble suspensions are less susceptible to surface contaminants than those involving single bubbles, because contaminants will be caught on bubble surfaces and brought to the top of the channel over time.

Our experiments were conducted in an inclined channel 200 cm in height (x-direction) and 2 cm in width (z-direction), identical to those used in Zenit *et al.* (2001) and Zenit *et al.* (2004). In the y-direction, where the mean velocity gradient occurs, the wall-to-wall distance was 2 cm. These dimensions ensured that the flow in the channel was fully developed in the x-direction, and the change in flow properties in the z-direction was small. Therefore, the flow in the channel was approximately two-dimensional, which was similar to the condition in the simulations in which we assumed periodic conditions in the x- and z-directions. Nitrogen bubbles were generated from a hexagonal array of capillaries with inner diameters of 100 μm which occupied the entire cross-section of the bottom of the channel. This arrangement of capillaries ensured that the bubbles were uniformly distributed in the channel and minimized any circulation due to uneven bubble distribution. As the addition of magnesium sulphate to the glycerine–water mixtures changes the kinematic viscosity

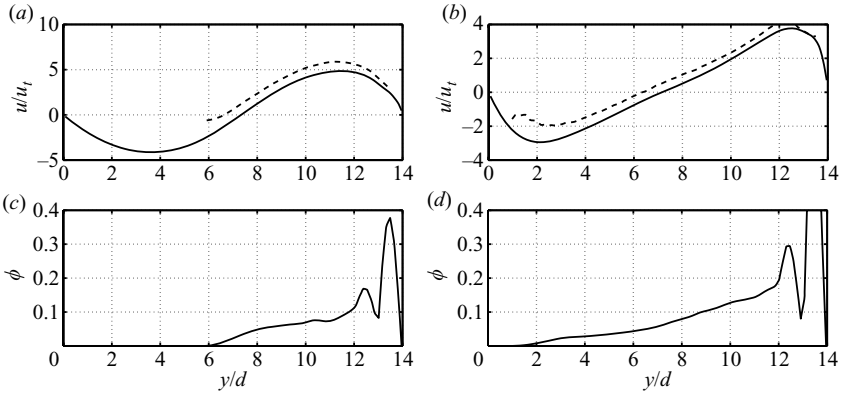

FIGURE 8. Examples of non-viscometric flows in inclined channels. Left: $Re = 20$, $\phi = 0.10$, and $\theta = 10^\circ$. Right: $Re = 0.1$, $\phi = 0.05$ and $\theta = 2^\circ$. (a, c) Velocity profiles, where the solid lines represent the velocity of the fluid phase and the broken lines represent the velocity of the bubble phase. (b, d) Volume fraction profiles. Here, the Reynolds numbers are based on the terminal velocities of the bubbles.

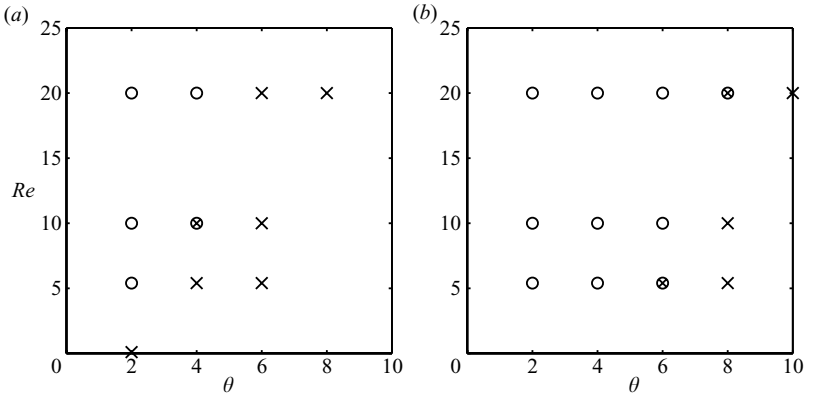

FIGURE 9. The parametric range in which simulations yield a viscometric shear flow in the middle of an inclined channel. (a) $\phi_0 = 0.05$; (b) $\phi_0 = 0.1$. The circles and $\times$ represent conditions for which viscometric and non-viscometric flows were obtained, and an overlayed circle and $\times$ represent a transition point ($|\phi - \phi_0|/\phi_0 \sim 0.1$ in the region $4 < y/d < 10$). Here the Reynolds numbers are defined based on the terminal velocity u_t.

of the fluid phase, we measured the kinematic viscosities of the mixtures using capillary viscometers (Cannon Instrument Company) that were kept in a water bath maintained at the temperature corresponding to the channel experiment. The temperature variation was approximately $\pm 1\,^\circ$C in the experiments and $\pm 0.2\,^\circ$C in the water bath. As simple inorganic electrolytes have very little effect on the surface tension of the solution (Weissenborn & Pugh 1996), we assumed that the surface tension in our glycerine–water–electrolyte solutions was the same as that in glycerine–water mixtures as measured by Maxworthy *et al.* (1996). The size and aspect ratios of the bubbles were measured by a digital camera (Panasonic FZ-15, 2304×1728 pixels, shutter speed $1/100$ s). A dual impedance probe was used to measure the bubble and volume fraction profiles as a function of y at the centreline $z = L_z/2$ and an x position 120 cm above the capillary array. We also used a high-speed video camera to measure the bubble velocity at $y = L_y/2$ at positions away from the centreline.

Exp. no.	1	2	3
Glycerine–water (% wt.)	61/39	56/44	51/49
Bubble diameter (mm)	1.46	1.56	1.44
Bubble aspect ratio	1.01	1.06	1.09
Kinematic viscosity ($m^2\,s^{-1}$)	2.48×10^{-5}	9.48×10^{-6}	6.71×10^{-6}
Temperature (°C)	22	21	21
Eo	0.36	0.38	0.33
Mo	2×10^{-5}	3×10^{-7}	6×10^{-8}
U_r (cm s^{-1})	3.3	9.2	7.5
α (s^{-1})	10.4	7.4	7.2
C_L^*	1.0	0.50	0.63
We	0.04	0.2	0.1
Ca	0.008	0.002	0.001
Ar	49.6	414	650
Re	2.1	12	16
Sr	0.45	0.12	0.14

TABLE 5. Summary of experimental conditions, measured mean relative velocity U_r and velocity gradient α, lift coefficient C_L^* and various dimensionless numbers. The channel inclination angle $\theta = 2°$; the average volume fraction $\phi_0 = 0.1$. The liquid phase contains 0.3 mol l^{-1} of magnesium sulphate. Although we do not have a direct measurement of the velocity of the liquid phase, based on simulation results we took the bubble velocities measured at the channel centreplane $y = L_y/2$ and averaged over three different z positions (centreline and ± 5 cm away from the centreline) and over time as U_r, and we took the gradient of bubble velocity in the y-direction as α. As the surface tension of simple, inorganic electrolyte solutions is not a strong function of electrolyte concentration (Weissenborn & Pugh 1996), the surface tension σ used to calculate *Eo*, *Mo*, *We* and *Ca* was obtained from tabulated values in Maxworthy *et al.* (1996).

In table 5, we list the fraction of glycerine and water in the fluid phase, the measured diameter and aspect ratio of bubbles, the kinematic viscosities, the temperatures in the channel and in the water bath and the Eötvös and Morton numbers. The bubbles were nearly monodisperse with mean diameters in the range of 1.4–1.6 mm with standard deviations of about 0.1 mm. In addition, the deformations of the bubbles were small. The ratio of channel gap thickness to bubble size was 13–14, which is close to the ratio of $L_y/d = 14$ used in the simulations. The Eötvös number was in the range 0.33–0.38; the Morton number ranged from 6×10^{-8} to 2×10^{-5}.

The channel was filled with glycerine–water–electrolyte solution to a height of 150 cm above the capillaries. The increase in the height of the free surface provided a means of determining the average volume fraction of the suspension. In our experiments, the average volume fraction ϕ_0 was held at 0.1 with an absolute error of approximately 0.01 due to variations in the gas pressure and uncertainties in the measurement of the height.

The volume fraction and bubble velocity were measured as a function of the y position, using a dual impedance probe. The impedance probe detects local changes in the electric resistance near the tip of the probe due to the passage of a bubble and registers this event as a peak in an otherwise relatively quiescent signal (Zenit *et al.* 2003). By measuring the fraction of time for which the signal is above a threshold, which can be obtained by calibrating the probe in a vertical channel with known bubble volume fraction, one can obtain the local volume fraction near the tip of the probe. When two such probes are separated in the x-direction by a small distance, one can obtain the time-averaged velocity of the bubbles at y from the time delay, which yields a peak cross-correlation between the two signals.

Because the signal to noise ratio depends on the availability and mobility of current-conducting ions, impedance probes are the most effective in electrolyte solutions. In the experiments by Zenit *et al.* (2001, 2004), a small amount of magnesium sulphate ($0.05\,\mathrm{mol\,l^{-1}}$) was used in an aqueous solution to suppress bubble coalescence and enhance the electrical conductivity. In our experiments, because glycerine–water mixtures are more viscous, ions were less mobile, and we had to increase the concentration of ions to obtain good electrical conductivity. Therefore, we used a relatively high magnesium sulphate concentration of $0.3\,\mathrm{mol\,l^{-1}}$. Two impedance probes were separated by a small distance 1.4 mm in the x-direction at $x = 120\,\mathrm{cm}$ and $z = L_z/2$. In order to obtain the profiles of bubble volume fraction and velocity, the probes were traversed in the y-direction with an accuracy of $\pm 0.2\,\mathrm{mm}$. A sampling frequency of 10 kHz provided sufficient temporal resolution to detect the cross-correlation, and a sampling time of 52.4 s, sufficient to measure hundreds of bubble passages, provided good statistical accuracy.

The volume fraction and bubble velocity profiles were measured for bubble suspensions in 61/39, 56/44 and 51/49 (% weight) mixtures of glycerine and water. Figure 10 shows the volume fraction and bubble velocity profiles measured in these suspensions. The volume fraction in the middle of the suspension was clearly constant at the two higher Reynolds numbers. It is possible that there was some variation of volume fraction in the most viscous suspension. However, the impedance signal was not as strong for this case, and this may have affected the accuracy of the impedance probes. The bubble velocities were fitted fairly well by linear functions of y in the middle of the channel, suggesting that the bubble flow resembled that obtained in the simulations. The simulations indicated that the bubble and fluid velocity profiles (and the relative velocity constant) were parallel in the bulk region, so we assume that the fluid velocity gradient α required to obtain the lift coefficient is equal to the measured bubble velocity gradient. The 90 % uncertainty levels of α are about 10–15 % of the mean values shown in figure 10 and table 5. The peak and trough in bubble velocity near the walls predicted by the simulations (cf. figure 2) cannot be detected in the experiments due to interference of the measurement if the tips of the probes are too close to the wall.

In order to determine the lift force coefficient C_L^* from the experiments using (3.1), one needs to know the velocity gradient α, the inclination angle θ, and the relative velocity U_r. Of these three parameters, θ is an input parameter of the system, and the velocity gradient α can be obtained from the linear regression just described. We did not have a direct measure of U_r in our experiments. However, as the simulations indicated that the bubble velocity on the plane of $y = L_y/2$ is very close to U_r, as one might expect from symmetry, we used the bubble velocity measured on the plane $y = L_y/2$ and averaged over three different z positions to approximate U_r. These z positions included the centreline $z = L_z/2$, where the bubble velocity could be directly obtained from the impedance probe, and two positions $\pm 5\,\mathrm{cm}$ away from the centreline, where the bubble velocities were obtained by selectively focusing the high speed video camera to the plane of $y = L_y/2$, then measuring the velocities of the bubbles that are in focus. The velocities measured at the two side positions were generally the same as that measured at the centreline, except for the case of the highest Re, where it was observed that the velocities at the two side positions were about 0.3–0.5 $\mathrm{cm\,s^{-1}}$ less than that at the centreline.

In table 5, we summarize the relative velocities and velocity gradients measured in the channel and the corresponding dimensionless numbers Re and Sr. The Reynolds numbers based on U_r were approximately 2.1, 12 and 16, and Sr varied between

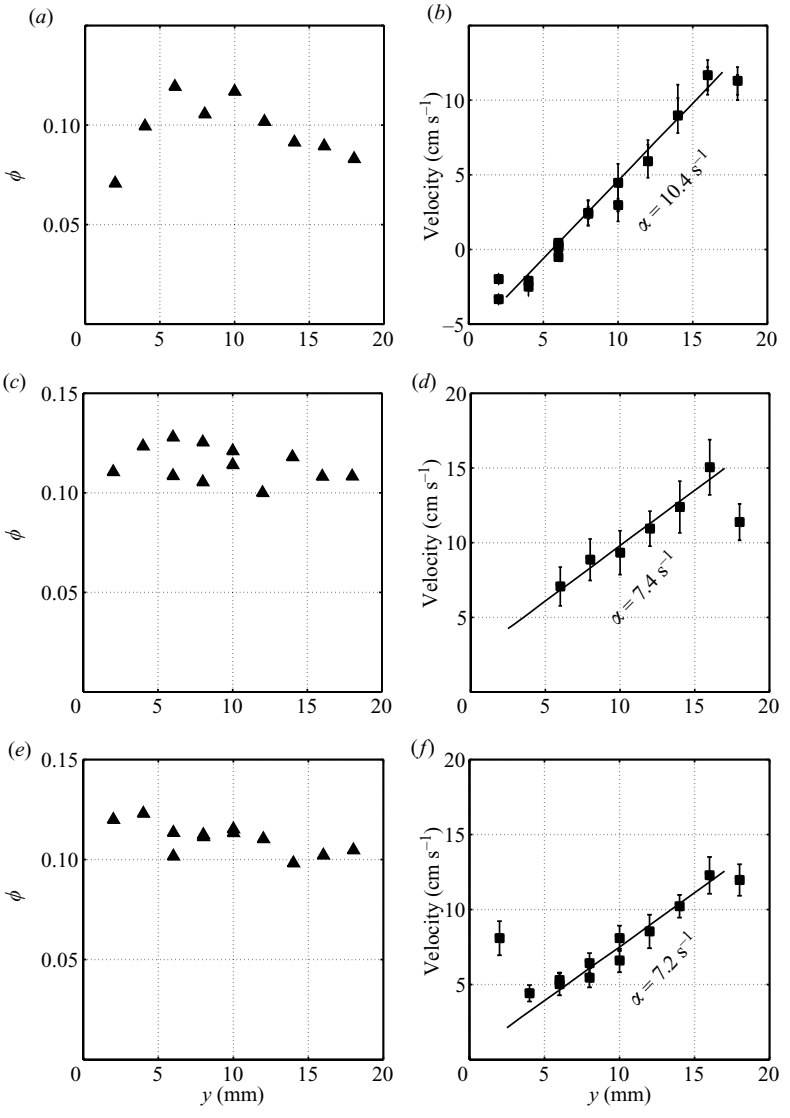

FIGURE 10. The volume fraction and bubble velocity profiles measured from experiments. The Reynolds numbers were 2.1 in (a,b), 12 in (c,d) and 16 in (e,f): (a), (c) and (e) are volume fraction profiles; (b), (d) and (f) are bubble velocity profiles. The solid lines accompanying the velocity profiles are the best linear fits, the slopes of which are also given in the plots. The error bars in the velocity profiles represent 90 % confidence intervals.

0.14 and 0.45. The lift force coefficients C_L^* in the three suspensions, from the most viscous one to the least viscous one, were 1.0, 0.50 and 0.63. In figure 11, we plot C_L^* obtained from experiments and simulations and compare them to C_L of an isolated bubble from (1.2) (Legendre & Magnaudet 1998). The error bars on the experimental data points are 90 % confidence intervals with the primary uncertainty arising from the measurement of the relative velocity U_r. The lift coefficients C_L^* obtained from the simulations lie within the error bars of the experiments. Both simulation and experiment indicate that the lift coefficient in the suspension is higher than that computed for an isolated bubble, and both show a decrease in lift coefficient as the

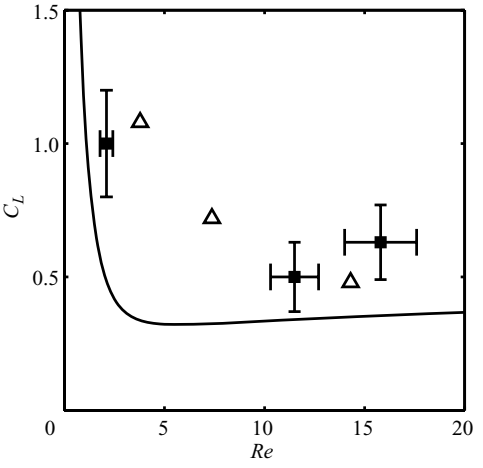

FIGURE 11. The lift force coefficients in an inclined channel with $\phi = 0.1$ and $\theta = 2^\circ$. The triangles and squares are lift force coefficients obtained from simulations and experiments in a suspension with volume fraction of 0.10. The error bars represent 90 % confidence intervals. The solid line corresponds to C_L of an isolated bubble calculated from (1.2), using $Sr = 0.2$.

Reynolds number is increased from a small value (2–5) to a more moderate value (7–16). Finally, we calculated the capillary numbers and the Weber numbers that are related to the deformability of the bubbles: $0.001 \leqslant Ca \leqslant 0.008$ and $0.04 \leqslant We \leqslant 0.2$. The small values of Ca and We suggest that the effect of deformation was not important in our experiments.

5. Summary

We have shown that a nearly viscometric shear flow of a homogeneous suspension of monodisperse spherical bubbles can be generated in the middle of a slightly inclined channel. In the viscometric shear region, the lateral force balance on the bubbles only involves the lift force from the shear and the small gravity component from the small angle of inclination. Using this simple force balance, the lift force coefficient for a spherical bubble in a sheared suspension was determined. Through simulations, we characterized the lift force coefficient C_L^* as a function of the Reynolds number Re, the dimensionless shear rate Sr and the average bubble volume fraction ϕ_0. We found that C_L^* is always higher than the lift force coefficient C_L for isolated spherical bubbles. The difference between C_L^* and C_L increases with increase in volume fraction and decreases with increase in Re and Sr.

The viscometric shear observed in our simulations is driven by thin bubble-rich and bubble-depleted regions near the upper and lower channel walls that form as a result of the cross-stream buoyancy force. The difference of the buoyancy force in these regions from that in the bulk exerts a force moment on the bulk suspension that drives a shear flow. This shear flow creates a lift force on the bubbles in the bulk that balances the cross-stream buoyancy force, preventing further bubble migration. The simple linear profile of the bubble and liquid velocities and the homogeneity of the bubble volume fraction in the bulk imply the absence of disperse-phase stress gradients, so that the y-momentum balance involves only the lift and buoyancy forces, allowing a simple measurement of the lift force coefficient in a bubble suspension. We mapped the region of parameter space for which such a simple viscometric flow

occurs using a criterion that the bubble volume fraction must not vary significantly within the bulk suspension.

In order to compare with simulations, we conducted a parallel experiment in a slightly inclined channel in which $\theta = 2^\circ$ and $\phi = 0.1$. We used glycerine–water mixtures in our experiments to make sure that the Reynolds numbers in the experiments fell within the range considered in the simulations. The measured bubble volume fraction and velocity profiles support the finding from the simulations that there is a nearly viscometric shear flow in the middle of the channel. The effective lift force coefficients from the experiments were in qualitative agreement with those from the simulations and were systematically larger than those for isolated bubbles.

Why would hydrodynamic interactions among bubbles enhance the lift force and increase the lift force coefficient? Before we attempt to answer this question, it is worthwhile to discuss the origin of the lift force and the various contributing factors. As discussed in Legendre & Magnaudet (1998), the lift force acting on a spherical bubble results from the asymmetric advection of the vorticity by the mean shear flow. In the low but finite Reynolds number regime ($Re < 5$), the vorticity surrounding the bubble comes primarily from the surface of the bubble and is proportional to the viscous drag. In the high-Reynolds-number limit ($Re > 20$), however, the unperturbed shear flow becomes the main source of vorticity, and it has been shown that for inviscid potential flows the lift force coefficient equals the added-mass coefficient (e.g. Auton 1987; Zhang & Prosperetti 1994; Wells 1996; Kang *et al.* 1997; Spelt & Sangani 1998), the value of which, for the case of a spherical bubble, is $1/2$. In the intermediate-Reynolds-number regime that we study ($5 < Re < 20$), it is expected that viscous drag and mean flow are equally important in generating the vorticity that is needed to produce the lift force. As both viscous drag and added mass increase with increasing bubble volume fraction, it is not surprising that the lift force also increases with increasing bubble volume fraction. For inviscid potential flows, the dependence of the added-mass coefficient C_a on the volume fraction has been well characterized. For example in dilute suspensions, van Wijngaarden (1976) predicted that $C_a = (1 + 2.76\phi)/2$, when bubbles are accelerated by equal forces, and Biesheuval & Spoelstra (1989) predicted that $C_a = (1 + 3.32\phi)/2$, when bubbles are subjected to equal accelerations. These formulae indicate that in a high-Re bubble suspension of 5 % volume fraction, C_a will be 14–16 % higher than that in the dilute limit. Indeed, when $Ar = 451$ and $\phi_0 = 0.05$ ($Re = 16$), we observed a 16 % increase in the lift force coefficient. This agreement in the percentage increase of C_a and C_L^* is probably fortuitous, as we have not considered the viscous effect that is a function of the Reynolds number: a decrease in Re would make bubble–bubble interaction stronger and its range longer and increase the sensitivity of C_L^* to ϕ as evidenced by our numerical data. Nevertheless, such an analysis can help us achieve a qualitative understanding of why the lift force is enhanced by the hydrodynamic interaction in a non-dilute bubble suspension.

This work was supported by NASA grant number NAG-1853. The computational work made use of the facilities of the Cornell Theory Center.

REFERENCES

Auton, T. R. 1987 The lift force on a spherical body in a rotational flow. *J. Fluid Mech.* **197**, 241–257.

Biesheuval, A. & Spoelstra, S. 1989 The added mass coefficient of a dispersion of spherical gas bubbles in liquid. *Intl J. Multiphase Flow* **15**, 911–924.

Bulthuis, H. F., Prosperetti, A. & Sangani, A. S. 1995 'Particle stress' in disperse two-phase potential flow. *J. Fluid Mech.* **294**, 1–16.

Bunner, B. & Tryggvason, G. 2003 Effect of bubble deformation on the properties of bubbly flows. *J. Fluid Mech.* **495**, 77–118.

Chen, A. U., Notz, P. K. & Basaran, O. A. 2002 Computational and experimental analysis of pinch-off and scaling. *Phys. Rev. Lett.* **88**, 174501.

d'Humières, D., Ginzburg, I., Krafczyk, M., Lallemand, P. & Luo, L.-S. 2002 Multiple-relaxation-time lattice Boltzmann models in three dimensions. *Phils. Trans. R. Soc.* A **360**, 437–451.

Kang, S.-Y., Sangani, A. S., Tsao, H.-K. & Koch, D. L. 1997 Rheology of dense bubble suspensions. *Phys. Fluids* **9** (6), 1540–1561.

Kim, S. & Karrila, S. J. 2005 *Microhydrodynamics: Principles and Selected Applications*. Dover.

Ladd, A. J. C. 1994*a* Numerical simulations of particulate suspensions via a discretized Boltzmann equation. Part 1. Theoretical foundation. *J. Fluid Mech.* **271**, 285–309.

Ladd, A. J. C. 1994*b* Numerical simulations of particulate suspensions via a discretized Boltzmann equation. Part 2. Numerical results. *J. Fluid Mech.* **271**, 311–339.

Ladd, A. J. C. & Verberg, R. 2001 Lattice-Boltzmann simulations of particle–fluid suspensions. *J. Stat. Phys.* **104**, 1191–1251.

Legendre, D. & Magnaudet, J. 1997 A note on the lift force on a bubble or a drop in a low-Reynolds-number shear flow. *Phys. Fluids* **9**, 3572–3574.

Legendre, D. & Magnaudet, J. 1998 Lift force on a bubble in a viscous linear shear flow. *J. Fluid Mech.* **368**, 81–126.

Lessard, R. R. & Zieminski, S. A. 1971 Bubble coalescence and gas transfer in electrolitic aqueous solutions. *Ind. Engng Chem. Fundam.* **10**, 260–269.

Lighthill, M. J. 1956 Drift. *J. Fluid Mech.* **1**, 31–53.

Magnaudet, J. & Eames, I. 2000 The motion of high-Reynolds-number bubbles in inhomogeneous flows. *Annu. Rev. Fluid Mech.* **32**, 659–708.

Maxworthy, T., Gnann, C., Kürten, M. & Durst, F. 1996 Experiments on the rise of air bubbles in clean viscous liquids. *J. Fluid Mech.* **321**, 421–441.

McLaughlin, J. B. 1991 Inertial migration of a small sphere in linear shear flows. *J. Fluid Mech.* **224**, 261–274.

Nguyen, N.-Q. & Ladd, A. J. C. 2002 Lubrication corrections for lattice-Boltzmann simulations of particle suspensions. *Phys. Rev.* E **66**, 046708.

Rensen, J., Bosman, D., Magnaudet, J., Ohl, C.-D., Prosperetti, A., Tögel, R., Versluis, M. & Lohse, D. 2001 Spiraling bubbles: how acoustic and hydrodynamic forces compete. *Phys. Rev. Lett.* **86**, 4819–4822.

Saffman, P. G. 1965 The lift force on a small sphere in a slow shear flow. *J. Fluid Mech.* **22**, 385–400.

Sangani, A. S. & Acrivos, A. 1983 Creeping flow through cubic arrays of spherical bubbles. *Intl J. Multiphase Flow* **9**, 181–185.

Sangani, A. S. & Didwania, A. K. 1993 Dispersed-phase stress tensor of bubbly liquids at large Reynolds numbers. *J. Fluid Mech.* **248**, 27–54.

Sangani, A. S. & Mo, G. 1994 Inclusion of lubrication forces in dynamical simulations. *Phys. Fluids* **6**, 1653–1662.

Sankaranarayanan, K. & Sundaresan, S. 2002 Lift force in bubbly suspensions. *Chem. Engng Sci.* **57**, 3521–3542.

Spelt, P. D. M. & Sangani, A. S. 1998 Properties and averaged equations for flows of bubbly liquids. *Appl. Sci. Res.* **58**, 337–386.

Sridhar, G. & Katz, J. 1995 Drag and lift forces on microscopic bubbles entrained by a vortex. *Phys. Fluids* **7**, 389–399.

Taylor, G. I. 1932 The viscosity of a fluid containing small drops of another fluid. *Proc. R. Soc. Lond.* A **138**, 41–48.

Tomiyama, A., Tamai, H., Zun, I. & Hosokawa, S. 2002 Transverse migration of single bubbles in simple shear flows. *Chem. Engng Sci.* **57**, 1849–1858.

Tsao, H.-K. & Koch, D. L. 1994 Collisions of slightly deformable, high Reynolds number bubbles with short-range repulsive forces. *Phys. Fluids* **6**, 2591–2605.

Van Nierop, E. A., Luther, S., Bluemink, J. J., Magnaudet, J., Prosperetti, A. & Lohse, D. 2007 Drag and lift forces on bubbles in a rotating flow. *J. Fluid Mech.* **571**, 439–454.

Weissenborn, P. K. & Pugh, R. J. 1996 Surface tension of aqueous solutions of electrolytes: Relationship with ion hydration, oxygen solubility, and bubble coalescence. *J. Colloid Interface Sci.* **14**, 550–563.

Wells, J. C. 1996 A geometrical interpretation of force on a translating body in rotational flow. *Phys. Fluids* **8**, 442–450.

van Wijngaarden, L. 1976 Hydrodynamic interactions between bubbles in liquid. *J. Fluid Mech.* **77**, 27–44.

Yin, X. 2007 Structure-property relations in bubble and solid particle suspensions with moderate Reynolds numbers. PhD thesis. Cornell University, Ithaca, NY, USA.

Yin, X., Koch, D. L. & Verberg, R. 2006 Lattice-Boltzmann method for simulating spherical bubbles with no-tangential stress boundary conditions. *Phys. Rev.* E **73**, 026301.

Zenit, R., Koch, D. L. & Sangani, A. S. 2001 Measurements of the average properties of a suspension of bubbles rising in a vertical channel. *J. Fluid Mech.* **429**, 307–342.

Zenit, R., Koch, D. L. & Sangani, A. S. 2003 Impedance probe to measure local gas volume fraction and bubble velocity in a bubbly liquid. *Rev. Sci. Instrum.* **74**, 2817–2827.

Zenit, R., Tsang, Y. H., Koch, D. L. & Sangani, A. S. 2004 Shear flow of a suspension of bubbles rising in an inclined channel. *J. Fluid Mech.* **515**, 261–292.

Zhang, D. Z. & Prosperetti, A. 1994 Averaged equations for inviscid disperse two-phase flow. *J. Fluid Mech.* **267**, 185–219.